

Main Determinants of Presynaptic Ca^{2+} Dynamics at Individual Mossy Fiber–CA3 Pyramidal Cell Synapses

Ricardo Scott and Dmitri A. Rusakov

Institute of Neurology, University College London, London WC1N 3BG, United Kingdom

Synaptic transmission between hippocampal mossy fibers (MFs) and CA3 pyramidal cells exhibits remarkable use-dependent plasticity. The underlying presynaptic mechanisms, however, remain poorly understood. Here, we have used fluorescent Ca^{2+} indicators Fluo-4, Fluo-5F, and Oregon Green BAPTA-1 to investigate Ca^{2+} dynamics in individual giant MF boutons (MFBs) in area CA3 traced from the somata of granule cells held in whole-cell mode. In an individual MFB, a single action potential induces a brief peak of free Ca^{2+} (estimated in the range of 8–9 μM) followed by an elevation to ~ 320 nM, which slowly decays to its resting level of ~ 110 nM. Changes in the somatic membrane potential influence presynaptic Ca^{2+} entry at proximal MFBs in the hilus. This influence decays with distance along the axon, with a length constant of ~ 200 μm . In giant MFBs in CA3, progressive saturation of endogenous Ca^{2+} buffers during repetitive spiking amplifies rapid Ca^{2+} peaks and the residual Ca^{2+} severalfold, suggesting a causal link to synaptic facilitation. We find that internal Ca^{2+} stores contribute to maintaining the low resting Ca^{2+} providing $\sim 22\%$ of the buffering/extrusion capacity of giant MFBs. Rapid Ca^{2+} release from stores represents up to 20% of the presynaptic Ca^{2+} transient evoked by a brief train of action potentials. The results identify the main components of presynaptic Ca^{2+} dynamics at this important cortical synapse.

Key words: synaptic transmission; synaptic plasticity; presynaptic regulation; calcium; CA3; hippocampus

Introduction

Mechanisms of Ca^{2+} -dependent neurotransmitter release are central to understanding synaptic function. Studies in giant calyceal terminals in the brainstem have provided critical insights into the underlying molecular machinery (Schneggenburger et al., 2002; von Gersdorff and Borst, 2002; Meinrenken et al., 2003). Similar advances with regard to cortical synapses have been made possible in large part by single-synapse imaging in the neocortex (Koester and Sakmann, 2000; Koester and Johnston, 2005) and whole-terminal recordings from giant mossy fiber (MF) boutons (MFBs) in the hippocampus (Geiger and Jonas, 2000; Engel and Jonas, 2005). Synapses formed by giant MFBs on CA3 pyramidal cells have also been intensely studied because they exhibit unusual short-term facilitation (Griffith, 1990) and an NMDA receptor-independent form of long-term potentiation (Zalutsky and Nicoll, 1990).

Several candidate mechanisms of short-term facilitation at these synapses have been proposed. Recordings from giant MFBs show that action potentials (APs) broaden during repetitive spiking, thus boosting presynaptic Ca^{2+} influx (Geiger and Jonas, 2000; Bischofberger et al., 2002). However, at moderate frequencies (10–30 Hz), this enhancement, in terms of either Ca^{2+} cur-

rent amplitude or transferred charge, amounts to only $<10\%$ during the first 10 spikes (Geiger and Jonas, 2000). A 10% increase in presynaptic Ca^{2+} entry is expected to augment postsynaptic responses in CA3 pyramidal cells less than to the second power (Geiger and Jonas, 2000; Blatow et al., 2003; Mori-Kawakami et al., 2003) or by $<21\%$. AP broadening alone thus cannot fully account for the profound synaptic facilitation routinely observed at similar frequencies.

Another candidate mechanism involves progressive saturation of endogenous Ca^{2+} buffers (Rozov et al., 2001). In young rodents, increasing the MF buffering capacity with Ca^{2+} chelators EGTA (high concentration) or BAPTA reduces short-term facilitation or paired-pulse ratios of postsynaptic responses (Regehr et al., 1994; Blatow et al., 2003; Mori-Kawakami et al., 2003). However, the effect is small in mature animals (Mori-Kawakami et al., 2003) and the residual presynaptic Ca^{2+} facilitates faster than do synaptic responses (Regehr et al., 1994). Furthermore, single-cell measurements of the main MF endogenous Ca^{2+} buffer calbindin-28K suggest that buffer saturation cannot explain strong facilitation of presynaptic Ca^{2+} (Muller et al., 2005).

An additional mechanism of short-term enhancement relies on presynaptic kainate receptors (Contractor et al., 2001; Lauri et al., 2001; Schmitz et al., 2001; Kamiya et al., 2002), which have been implicated in triggering Ca^{2+} release from Ca^{2+} stores (Liang et al., 2002; Lauri et al., 2003). However, AP-driven Ca^{2+} responses recorded in multiple MFs appear insensitive to Ca^{2+} store blockade (Carter et al., 2002; Breustedt and Schmitz, 2004).

In summary, the machinery of presynaptic Ca^{2+} signaling at MF synapses remains poorly understood. Because optical recordings from tissue-loaded MFs do not report resting Ca^{2+} levels

Received Nov. 21, 2005; revised May 24, 2006; accepted May 24, 2006.

This work was supported by the Wellcome Trust, the Medical Research Council UK, the European Union (HPRN-CT-2000-00082; PROMEMORIA LSHM-CT-2005-512012), and the Human Frontier Science Program. We thank Dimitri Kullmann, Kirill Volynsky, Alex Verkhratsky, and colleagues at University College London for valuable comments on this manuscript.

Correspondence should be addressed to Dmitri A. Rusakov, Institute of Neurology, University College London, Queen Square, London WC1N 3BG, UK. E-mail: d.rusakov@ion.ucl.ac.uk.

DOI:10.1523/JNEUROSCI.0946-06.2006

Copyright © 2006 Society for Neuroscience 0270-6474/06/267071-11\$15.00/0

and may incorporate signals from unidentified cellular structures, testing at the level of single synapses is preferable (Jackson and Redman, 2003; Ruiz et al., 2003). In addition, integrity of the presynaptic cell is important for quantitative evaluation of presynaptic Ca^{2+} signaling. Here, we combine two-photon microscopy with an improved slicing method, electrophysiology, and kinetic modeling to evaluate the role of somatic voltage, Ca^{2+} buffering, and Ca^{2+} stores in shaping Ca^{2+} dynamics in giant MFBs in area CA3 supplied by axons of intact granule cells.

Materials and Methods

Preparation and electrophysiology. Acute 300 μm hippocampal slices from 3- to 4-week-old male Sprague Dawley rats were transferred to a recording submersion-type chamber (Scientific Systems Design, Montclair, NJ), superfused with the following (in mM): 124 NaCl, 2 KCl, 2 CaCl_2 , 1 MgCl_2 , 26 NaHCO_3 , and 10 glucose, and bubbled with 95:5 of O_2/CO_2 . The slice cutting (close to the parasagittal plane) is detailed in Results. Internal solution included the following (in mM): 150 K methanesulfonate, 5 KCl, 10 HEPES, 3 MgATP_2 , and 0.4 GTP, and also included fluorophores as indicated. Unless specified otherwise, granule cells were held at -80 mV. Orthodromic action potentials or escape currents recorded in current- or voltage-clamp mode, respectively, were evoked by 2 ms command voltage pulses (single, 5, or 50, at 20 Hz, as indicated). Alternatively, 100 μs electrical stimuli were applied to stratum lucidum with a bipolar electrode. Recording sweeps (normally 500 ms long) were collected at a 5 kHz rate in 30 s or 1 min intervals using LabView (National Instruments, Austin, TX). Routinely, experiments were performed in the presence of 5 μM CGP-52432, 50 μM APV, and 100 μM picrotoxin at room temperature. Receptor antagonists were purchased from Tocris Cookson (Bristol, UK), and fluorescent probes were purchased from Invitrogen (San Diego, CA). All animal-handling procedures followed current United Kingdom regulations.

Two-photon excitation fluorescence imaging. Imaging experiments were performed using a multiphoton installation comprising a Radiance 2000 imaging system (Zeiss, Oberkochen, Germany) optically linked to a femtosecond laser MaiTai (SpectraPhysics, Mountain View, CA) and integrated with a single-cell electrophysiology setup (Rusakov and Fine, 2003). Granule cells were held in whole-cell mode and loaded with two fluorophores, a morphological tracer Alexa Fluor 594 (20 μM) and a Ca^{2+} indicator [Fluo-4, Fluo-5F, or Oregon Green BAPTA-1 (OGB-1), as specified]. In granule cells with intact axons (see Results) (supplemental Fig. 1, available at www.jneurosci.org as supplemental material), 15–20 min were initially allowed for indicator equilibration before switching the system into fluorescence mode to trace the axon into the stratum lucidum. Fluorophores were excited in two-photon mode at 810 nm, with the laser power optimized for emission detection at different depths in the slice.

The axon was followed from the soma into stratum lucidum using frame mode scanning (256×256 pixels, 500 Hz; the number of taken frames was kept small to minimize phototoxic damage) and the system was focused on a giant MFB identified by its distinct morphology, at the maximum optical resolution (~ 0.2 μm ; digital capture, 70 nm per pixel). Recording started when the baseline fluorescence in both channels was stable (~ 1 h later) (see Results) (supplemental Fig. 2, available at www.jneurosci.org as supplemental material); the experiment lasted for up to 3–4 h and dye equilibration was routinely controlled *post hoc*, by comparing the resting fluorescence of Alexa Fluor 594 at the end of the experiment with that recorded 1–1.5 h earlier. We conducted two additional tests to verify that Ca^{2+} indicators are equilibrated along the axon and are not extruded from the cells appreciably with time. In the first test, we carefully pulled out the patch pipette after initial dye equilibration. The seal was confirmed by the fact that we obtained outside-out patches as a result and that cells could respond to extracellular stimulation by generating action potential-dependent Ca^{2+} transients. The subsequent recordings indicated no detectable loss of the resting fluorescence F over 100–200 min (supplemental Fig. 3, available at www.jneurosci.org as

supplemental material). In the second test, we measured the baseline fluorescence in the axonal regions at different distances from the soma and found no spatial gradient (supplemental Fig. 4, available at www.jneurosci.org as supplemental material). The results of both tests argued against any significant loss of fluorescence indicators from the axon.

Fluorescence responses were recorded in line-scan mode at 500 Hz (500 or 1000 ms sweeps; intersweep interval, 30 s or 1 min) and stored for off-line analysis. The Ca^{2+} -dependent fluorescence response $\Delta F/F$ (integrated over the visible MFB width) was routinely calculated as follows: $(F_{\text{post}} - F_{\text{pre}})/(F_{\text{pre}} - F_0)$. The values of F_{pre} and F_{post} stand for the line-scan fluorescence averaged over, respectively, 100 ms before the first spike and either 50 ms in the case of single-response amplitude measurements or 250 ms in the case of five-response amplitude measurements (20 Hz train of five APs) after the first spike onset. F_0 denotes the background fluorescence measured outside any cell structures filled with the indicator. Because special care was taken to avoid escape of the indicator from the pipette, and because the site of imaging was hundreds of micrometers away from the pipette tip, F_0 was likely to represent the photomultiplier tube dark current. Image analyses were performed on stacks of stored line-scan images using a set of custom NIH Image macros. False color tables and averaged images were used for illustration purposes but the original (gray level) pixel brightness values in each line-scan image were used for the quantitative analysis. In most experiments, we reconstructed the axon trajectory using a collage of high-resolution Kalman-filtered z -stacks 15–20 μm deep. In total, we obtained full reconstruction of 43 axons, with an average distance between the recorded MFB and the soma of 686 ± 38 μm . Throughout the experiments, we observed no failures of spike-driven Ca^{2+} signals propagating along the main axonal trunk including giant MFBs. This, however, does not rule out the possibility that propagation could fail at higher spiking frequencies and/or in thin axon collaterals.

The two-photon excitation probability profile is proportional to the squared illumination light intensity I_{2p}^2 (Zipfel and Webb, 2001):

$$I_{2p}^2(u, v) = \left| 2 \int_0^1 J_0(v\rho) \exp\left(-\frac{i}{2}u\rho^2\right) \rho d\rho \right|^2, \quad (1)$$

where the canonical coordinates $u = 4k\sin^2(\alpha/2)z$ and $v = k\sin(\alpha)r$ represent the axial distance z ; the radial distance r ; the numerical aperture of the objective, $\text{NA} = \sin(\alpha) = 0.9$; and wave number $k = n(2\pi/\lambda)$ ($n = 1.33$ is the medium refraction index and $\lambda = 810$ nm is the wavelength); J_0 denotes zero-order Bessel's function of the first kind. This theoretical function, however, represents the lower-limit estimate of the excitation profile: in reality, optical aberrations and imperfect alignment of the experimental optical system are likely to increase the spread of excitation. Similar considerations apply to the emission path. We therefore obtained an estimate of the excitation–emission profile by recording the point-spread function (PSF) of the system using 0.17 μm fluorescent beads (PS-Speck Microscope Point Source kit; Invitrogen) as illustrated below.

Estimating the resting concentration of presynaptic Ca^{2+} . Classically, the resting Ca^{2+} level ($[\text{Ca}^{2+}]_{\text{rest}}$) can be estimated from the following relationship:

$$\frac{[\text{Ca}^{2+}]_{\text{rest}}}{K_d} = \frac{F - F_{\text{min}}}{F_{\text{max}} - F}, \quad (2)$$

where K_d is the Ca^{2+} indicator dissociation constant, and F_{max} , F , and F_{min} represent maximum, resting, and Ca^{2+} -independent fluorescence of the indicator.

However, the high dynamic range of Ca^{2+} indicators such as Fluo-4 implies that the resting fluorescence F could be comparable with the detection threshold of the system. In this case, the useful fluorescence signal could blend with the background noise in a nonlinear manner, which makes it difficult to obtain reliable ratios $\Delta F/F$ or F_{max}/F . This difficulty could be addressed by relating ΔF to the Ca^{2+} -independent fluorescence R recorded in the “red” (e.g., Alexa) channel (Oertner et al., 2002). We have modified this approach by diverting part of the Alexa Fluor 594 emission signal into the “green” Fluo-4 channel using a 560 nm dichroic mirror and a 700 nm short-pass filter. The use of the cross talk

Table 1. Adopted Ca^{2+} buffering constants in Ca^{2+} kinetics measurements (see Fig. 4)

Buffer	K_d (μM)	k_{on} ($\text{M}^{-1}\text{ms}^{-1}$)	k_{off} (ms^{-1})	Reference
Calbindin-28K	300 nM	3×10^4	9×10^{-3}	Nagerl et al., 2000; Berggard et al., 2002
Fluo-4	350 nM	6×10^5	0.21	Gee et al., 2000; Maravall et al., 2000
Fluo-5F	1 μM	3×10^5	0.3	Naraghi, 1997; Gee et al., 2000; Oertner et al., 2002; Sabatini et al., 2002

Alexa Fluor 594 signal, denoted here as R_{ct} , was advantageous because this (1) elevated emission in the Fluo-4 channel well above the detection threshold of the system (see above) and (2) allowed both the Ca^{2+} -dependent signal ΔF and R_{ct} to be recorded through the same channel. (This method, however, is unlikely to be advantageous when the useful resting green fluorescence is substantially above the background noise.) The average ratio $\langle R_{\text{ct}}/R \rangle$ was measured in separate experiments, by comparing emission in the two corresponding channels while imaging giant MFBs loaded with Alexa Fluor 594 only (see Results). In these terms, the recorded resting and maximum fluorescence (F and F_{max} , respectively) will include a Ca^{2+} -independent fluorescence fraction $R_{\text{ct}} + F_{\text{min}}$. Equation 2 can be therefore recast as follows:

$$\frac{[\text{Ca}^{2+}]_{\text{rest}}}{K_d} = \frac{F/F_{\text{max}} - \langle R_{\text{ct}}/R \rangle R/F_{\text{max}} - F_{\text{min}}/F_{\text{max}}}{1 - F/F_{\text{max}}}. \quad (3)$$

In the case of the high dynamic range indicator Fluo-4, $F_{\text{min}}/F_{\text{max}} \approx 0$ (Maravall et al., 2000; Oertner et al., 2002), implying that estimation of $[\text{Ca}^{2+}]_{\text{rest}}$ simply requires experimental measurements of R_{ct} and R , according to Equation 3. In the case of the lower dynamic range indicator OGB-1 ($K_d \approx 200$ nM), this equation also includes the known value of $F_{\text{max}}/F_{\text{min}} \approx 6$ (Maravall et al., 2000; Oertner et al., 2002; Jackson and Redman, 2003).

Nonstationary presynaptic Ca^{2+} kinetics. To translate the recorded fluorescence into the underlying Ca^{2+} kinetics, we used a single-compartment, multicomponent kinetic model (Helmchen et al., 1997; Neher, 1998; Jackson and Redman, 2003) in its nonstationary form, which requires no steady-state approximations (Sabatini and Regehr, 1998; Rusakov et al., 2005). Multicompartmental modeling was deemed unfeasible in the present study because (1) the Ca^{2+} fluorescence time course was indistinguishable between subregions inside a single bouton (the PSF of the system was too large to distinguish between such subregions) (see Fig. 4) and (2) Ca^{2+} exchange between multiple space partitions has little effect on the volume-average Ca^{2+} concentration transient (Sabatini and Regehr, 1998). Parameters of the model were constrained and cross-validated by (1) an independent estimate of $[\text{Ca}^{2+}]_{\text{rest}}$ (see above), (2) an independent estimate of the endogenous buffer (calbindin-28K) concentration (Jackson and Redman, 2003; Muller et al., 2005), and (3) comparing the effects of different configurations of Ca^{2+} indicators/buffers on the recorded fluorescence signal versus the predicted kinetics.

The finite-difference kinetic scheme explicitly included the rate of Ca^{2+} entry, j_{Ca} , the binding–unbinding reactions with the endogenous buffer (calbindin-28K) B and Ca^{2+} indicator I , and the Ca^{2+} removal rate P , according to the following equation:

$$\partial[\text{Ca}^{2+}]/\partial t = j_{\text{Ca}}(t) + k_{\text{off}}^I[\text{CaI}] + k_{\text{off}}^B[\text{CaB}] - P(t) - k_{\text{on}}^I[\text{Ca}^{2+}][I] - k_{\text{on}}^B[\text{Ca}^{2+}][B], \quad (4)$$

where brackets denote concentrations, CaI and CaB stand for the Ca-bound indicator and buffer, respectively, and the kinetic constants (top indices denote buffer B or indicator I ; bottom indices indicate on and off constants) are summarized in Table 1. The mass conservation rules are as follows:

$$[I]_{\text{tot}} = [\text{CaI}] + [I], [B]_{\text{tot}} = [\text{CaB}] + [B], \text{ and } [\text{Ca}]_{\text{tot}} = [\text{Ca}^{2+}] + [\text{CaB}] + [\text{CaI}], \quad (5)$$

where index “tot” denotes total amount. The AP-evoked Ca^{2+} influx rate j_{Ca} followed the Gaussian (Sabatini and Regehr, 1998; Rusakov et al., 2004) as follows:

$$j_{\text{Ca}} = \frac{\Delta[\text{Ca}^{2+}]_{\text{tot}}}{\sigma\sqrt{2\pi}} \exp\left(-\frac{(t - t_0)^2}{2\sigma^2}\right), \quad (6)$$

in line with experimental observations (Meinrenken et al., 2003), with the MFB spike half-width $\sigma \approx 0.5$ ms (Bischofberger et al., 2002), onset at t_0 , and the time integral of $\Delta[\text{Ca}^{2+}]_{\text{tot}}$ reflecting total Ca^{2+} entry. Removal of Ca^{2+} , which is a complex process involving diffusion, pumping out and/or sequestration was approximated by a first-order reaction (Jackson and Redman, 2003) (however, for discussion, see Matveev et al., 2004; Holzman et al., 2005) at the rate $P([\text{Ca}^{2+}] - [\text{Ca}^{2+}]_{\text{rest}})$ (Eq. 4). The model, therefore, operated with only two adjustable (free) parameters: $\Delta[\text{Ca}^{2+}]_{\text{tot}}$ and P . However, varying either $\Delta[\text{Ca}^{2+}]_{\text{tot}}$ or P had virtually independent effects on the calculated amplitude ($\Delta F/F$) and decay of fluorescent responses, respectively (see Results) (supplemental Fig. 5, available at www.jneurosci.org as supplemental material). Each of the two parameters could be therefore constrained by a straightforward fitting procedure that would match the calculated and the experimental fluorescence, as discussed previously (Rusakov et al., 2005).

Assessing calbindin-28K washout from the axon. Gradual washout of endogenous buffers in whole-cell mode could alter presynaptic Ca^{2+} dynamics in the recorded cell (Rozov et al., 2001; Blatow et al., 2003). A previous study has estimated that washout of the endogenous Ca^{2+} buffer calbindin-28K from the granule cell soma occurs with a time constant of ~ 9.7 min (Muller et al., 2005). To assess its washout rate at different regions of the axon, we used a multicompartmental diffusion model based on a detailed quantitative study of granule cell morphology (Claiborne et al., 1990). The modeled cell included the 19- μm -long/10- μm -wide elliptical soma and a 2000- μm -long/0.4- μm -thick axon. The average dendritic tree of granule cells (two primary dendrites, each ~ 2.5 μm in diameter, giving rise to an arbor spreading over ~ 300 μm with the total dendritic length of 3221 μm) (Claiborne et al., 1990) was represented by a single 300- μm -long trunk of the matching cross section (9.6 μm^2) and total volume (2900 μm^3). The patch pipette (tip diameter, 1.8 μm) provided a concentration clamp source linked to a somatic compartment. The initial calbindin concentration was 160 μM , and at $t = 0$, the concentration clamp was imposed through the pipette. Diffusion simulations were performed with the compartment size of 5 μm (464 compartments in total) using numerical algorithms described previously (Scimemi et al., 2004). The single unknown parameter, the effective diffusivity of calbindin was adjusted to obtain the best fit between the experimental data on somatic washout (Muller et al., 2005) and the computed calbindin concentration time course in the soma (supplemental Fig. 6, available at www.jneurosci.org as supplemental material). Under these conditions, washout of calbindin from the axonal regions where giant MFBs occur (the average distance from the soma, 686 ± 38 μm ; $n = 43$ fully reconstructed axons) is predicted in the range of $<5\%$ within 2–3 h after break-in (supplemental Fig. 6, available at www.jneurosci.org as supplemental material). This is consistent with the stable amplitude of recorded $\Delta F/F$ during that period (supplemental Fig. 2, available at www.jneurosci.org as supplemental material).

Average data are shown as mean \pm SEM; a t test was used for statistics.

Results

Tracing granule cell axons from the soma into the stratum lucidum

Obtaining connected granule cell–CA3 pyramidal cell pairs has been difficult in acute slices because of the intrinsically low probability of finding such connections through random sampling (Amaral et al., 1990). In addition, granule cell somata occur 200–300 μm outside the main MF projection plane (Tamamaki and Nojyo, 1991; Acsady et al., 1998) (Fig. 1A) and therefore are likely

to be cut off during preparation of slices that preserve MFs in the stratum lucidum. To reduce the chances of cutting granule cell axons close to the soma, hippocampal slices were sectioned at an angle (close to the parasagittal direction) to the plane of the main MF projections (Fig. 1*A,B*). We then loaded granule cells, in whole-cell mode, with two fluorescence indicators (see Materials and Methods) and monitored APs evoked antidromically in the soma by extracellular stimulation of the stratum lucidum. Although virtually all monitored cells generated APs, only a small proportion (<10%) showed an AP latency exceeding 3–4 ms in response to the minimum strength stimuli sufficient to generate an AP (Fig. 1*C*). On subsequent visual inspection in a microscope, only these cells projected their axon into area CA3 (Fig. 1*D*) (Alexa Fluor 594 channel); the axons of cells with a short AP latency were truncated at <200 μm from the soma. These observations suggested a simple electrophysiological test to facilitate selection of cells with long axons before imaging. In the microscope, giant MFs were identified in area CA3, >300 μm from the soma, by their distinctive large size (5–8 μm) and thin filopodial protrusions (Fig. 1*D,E*, image panels; supplemental Fig. 1, available at www.jneurosci.org as supplemental material).

We used 2 ms somatic depolarizing command voltage pulses to evoke orthodromic APs. These were rapidly followed by fluorescence transients in giant MFs (Fig. 1*F,G*). After a period of equilibration lasting 1 h or more depending on the distance from the soma, both Ca^{2+} -dependent and Ca^{2+} -independent fluorescence in giant MFs remained stable for several hours (supplemental Fig. 2, available at www.jneurosci.org as supplemental material). In contrast, proximal MF boutons tended to increase their baseline fluorescence, as well as their evoked Ca^{2+} responses, by the end of 30–40 min recording sessions in similar conditions (Ruiz et al., 2003); this is consistent with partial washout of endogenous buffers at short distances from the soma (Blatow et al., 2003; Muller et al., 2005), as discussed in Materials and Methods (supplemental Fig. 6, available at www.jneurosci.org as supplemental material).

Neither the amplitude nor the decay time of the AP-evoked fluorescence transients varied systematically with the distance from the soma in $n = 43$ giant MFs with fully reconstructed axons (Fig. 2*A,B*). In approximately one-third of all experiments, we compared Ca^{2+} responses evoked under voltage clamp ($V_h = -80$ mV) or current clamp (current adjusted to correspond to $V_m = -80$ mV). Because no consistent differences were found, the data from these experiments were pooled.

Electrotonic control of Ca^{2+} signaling in MFs

We have shown previously (Ruiz et al., 2003) that varying the somatic holding voltage modulates the AP-evoked presynaptic

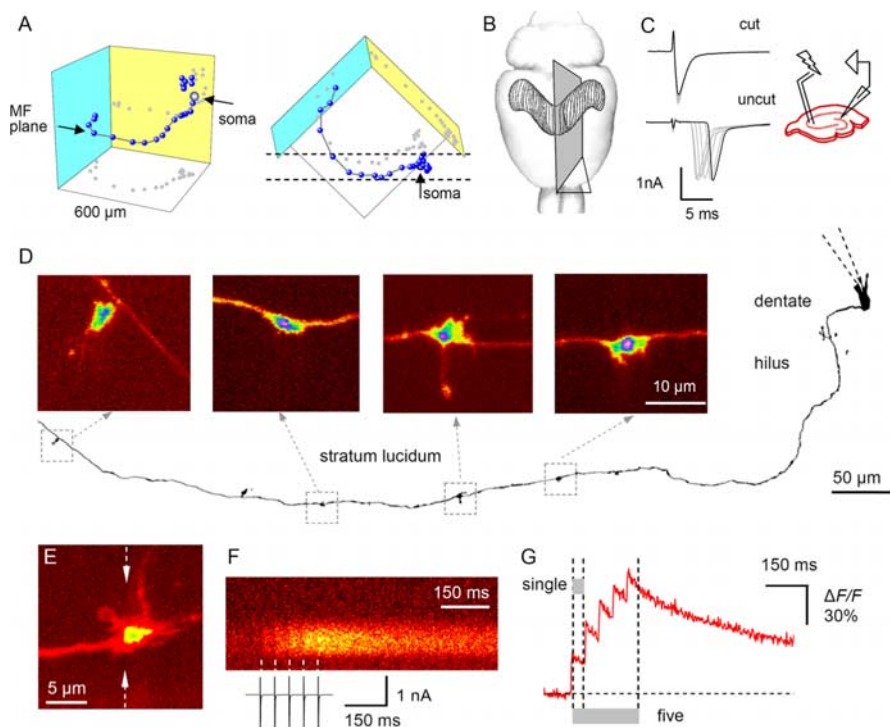


Figure 1. Two-photon excitation imaging of giant MFs projected by intact granule cells to stratum lucidum. *A*, Three-dimensional (3D) representation of the granule cell axon trajectory (blue connected spheres) reconstructed from a pair of orthogonal projections reported previously [Acasady et al. (1998), their Fig. 2*B*]. Disconnected blue spheres, Dendritic ends; gray-shaded dots, two orthogonal projections. Dashed lines in the right panel, Preferred slicing position showing the cutting planes normal to the plane of image. *B*, Positioning of the cutting blade with respect to the hippocampus, a 3D view (the rat brain silhouette is shown for reference); note the oblique cutting angle. *C*, Characteristic traces of antidromic action potentials (escape currents) evoked by stimulation of stratum lucidum (inset diagram) in cut and uncut axons identified by microscopy. The black traces correspond to the minimum stimulus intensity sufficient to generate a spike (the intensity depended on the juxtaposition of the electrode and the axon and varied between slices), and the gray traces correspond to further increases in the stimulus strength. Note a dramatic difference in the poststimulus latency between cut and intact axons. *D*, An example of the reconstructed granule cell axon; Alexa Fluor 594 channel, whole-cell mode (see Materials and Methods); the dashed frames and image panels illustrate four giant MFs (many thin filopodia are masked by the z-stack fusion image). *E*, A characteristic giant MF (for the full axon reconstruction, see supplemental Fig. 1, available at www.jneurosci.org as supplemental material); the arrows here and in subsequent figures represent the line scan position. *F*, Line-scan recording (Fluo-4 channel; 500 Hz) following five APs at 20 Hz; average of five sweeps. *G*, Line-scan fluorescence time course; the dashed lines and gray segments represent integration windows for single-pulse and five-pulse $\Delta F/F$ measurements.

Ca^{2+} transient up to 40% in MF axonal boutons in the hilus (Fig. 2*C*). We found, however, that Ca^{2+} signals at giant MFs were unaffected by changing the holding voltage (Fig. 2*D*) ($n = 8$). To determine the extent of the somatic electrotonic influence in our conditions, we repeated these experiments in proximal axonal boutons (Fig. 2*C*). Changing the somatic voltage between -110 and -60 mV resulted in a Ca^{2+} signal variation, cast in relative terms as $\text{var}_V(\Delta F/F) = (\text{Max } \Delta F/F - \text{Min } \Delta F/F) / \text{Max } \Delta F/F$ (Fig. 2*D*), of $19 \pm 3\%$ ($n = 11$) (Fig. 2*E*). Surprisingly, this influence was only one-half of that detected in the previous study where $\text{var}_V(\Delta F/F)$ was $\sim 40\%$ (Ruiz et al., 2003).

This discrepancy, however, has a simple explanation: the previous study dealt with axons cut, on average, at 100–150 μm from the soma, whereas the present experiments were performed on cells with intact axons. According to cable theory, cutting and sealing the axon increases its electrotonic space constant, thus facilitating remote voltage control. [Although open-ended axons would have a different effect on the length constant, they are unlikely to be compatible with cell survival; in addition, sealed axonal ends, with no detectable escape of fluorescence, were routinely observed in a microscope and the intracellular level of Al-

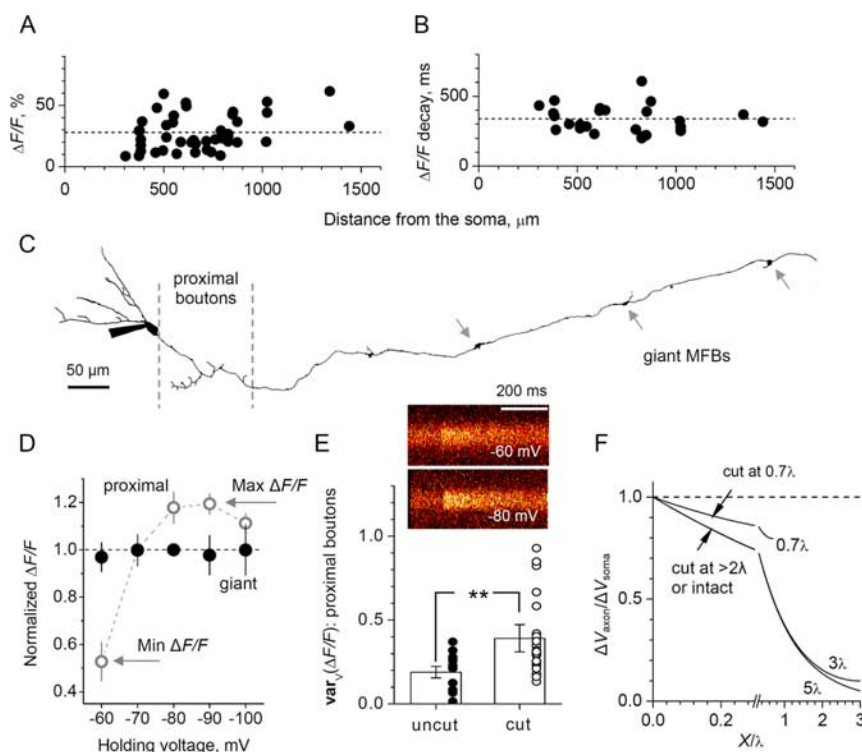


Figure 2. Differential electrotonic control of presynaptic Ca^{2+} signaling in hilar and CA3 MF boutons. **A, B**, Amplitude (**A**) and decay time constant (**B**) of the Ca^{2+} -dependent fluorescence signal induced in individual giant MFs by a single orthodromic AP. The values are plotted against the distance from the soma (average, $686 \pm 38 \mu\text{m}$; $n = 43$). The dashed lines indicate average values: $\Delta F/F = 28 \pm 2\%$ ($n = 43$); decay constant, $339 \pm 19 \text{ ms}$ ($n = 26$); decay constant estimates in the remaining MFs were unreliable because of the low signal-to-noise ratio: the cells were discarded if the outcome of single-exponent fitting changed by $>20\%$ depending on the sampling time window). **C**, An example of the reconstructed granule cell axon (Alexa Fluor 594 channel; whole-cell mode). The dashed lines indicate location of proximal boutons; the arrows indicate giant MFs. **D**, $\Delta F/F$ amplitude (relative values) versus somatic holding voltage; filled circles, giant MFs ($n = 8$); open circles, data from proximal en passant boutons (Ruiz et al., 2003) ($n = 15$). The arrows depict the average maximum and minimum Ca^{2+} -dependent signals, Max $\Delta F/F$ and Min $\Delta F/F$, respectively. The error bars in **D** and **E** represent SEM. **E**, Image panels, A single-cell line-scan example depicting Max $\Delta F/F$ and Min $\Delta F/F$ signals in the same giant MFs at -80 mV and -60 mV , respectively. Plot, The average normalized Min–Max range of the fluorescence response $\text{var}_V(\Delta F/F) = (\text{Max } \Delta F/F - \text{Min } \Delta F/F) / \text{Max } \Delta F/F$ in proximal boutons of intact axons ($19 \pm 3\%$; $n = 11$; filled circles) and cut axons ($39 \pm 8\%$; $n = 22$; open circles; $**p < 0.01$). **F**, The “local-to-clamped” voltage ratio V/V_0 plotted against the distance to the voltage-clamped soma along the axon (equivalent cable), according to Equation 7; distances are measured in electrotonic length units X/λ ; the plotted lines are marked with the corresponding axon length value, L . For the axons cut at $L > 2\lambda$, the curves are indistinguishable in the somatic vicinity ($L < \lambda$). The arrows illustrate that cutting a long axon at $\sim 0.7\lambda$ improves local voltage-clamp control approximately twofold.

exa Fluor 594 was unchanged throughout the experiment (supplemental Fig. 2, available at www.jneurosci.org as supplemental material).] Indeed, when we recorded from proximal boutons in cells that had their axons cut off 100–150 μm from the soma ($n = 7$), the values of $\text{var}_V(\Delta F/F)$ were indistinguishable from the previous results (Ruiz et al., 2003); combining the current and previous data in the cut axons gave an average $\text{var}_V(\Delta F/F)$ of $39 \pm 8\%$ ($n = 22$) (Fig. 2E).

We used the observed twofold difference in $\text{var}_V(\Delta F/F)$ between cut and uncut axons to estimate the electrotonic space constant of the axon. In an equivalent cable approximation, the steady-state voltage V at a distance x from a point clamped at V_0 is given by the following relationship (for discussion, see Jackson, 1992):

$$\frac{V(X)}{V_0} = \frac{\cosh(L - X)}{\cosh(L)}, \quad (7)$$

where X and L represent distance x and the axon length l , respectively, cast in terms of the space constant λ : $X = x/\lambda$ and $L = l/\lambda$ (Fig. 2F). This relationship predicts that, to reduce the extent of

somatic voltage control approximately twofold, one has to cut the long axon at $L \sim 0.7\lambda$ (Fig. 2F, arrows). Because the actual MF axons were cut at $L \approx 100$ – $150 \mu\text{m}$ in these experiments, the estimated MF axon space constant was $\lambda = L/0.7 = 150$ – $200 \mu\text{m}$. This value is consistent with electrotonic isolation of Ca^{2+} transients in the giant MFs (Fig. 2D), also indicating that MF synapses in the hilus could be affected by the granule cell resting somatic voltage.

Resting Ca^{2+} concentration at giant MFs

To estimate $[\text{Ca}^{2+}]_{\text{rest}}$ from Equation 3, we first measured the cross-talk fraction of Alexa Fluor 594 fluorescence in the Fluo-4 (Ca^{2+} signal) emission channel, R_c/R . Granule cells were loaded with 20 μM Alexa Fluor 594, and MFs were imaged in both channels (Fig. 3A, B). Comparing direct versus cross-talk signals of Alexa Fluor 594 indicated an average R_c/R ratio of 0.035 ± 0.002 ($n = 24$) (Fig. 3C). We then loaded cells with 200 μM Fluo-4 (in addition to 20 μM Alexa) and, after indicator equilibration (supplemental Fig. 2, available at www.jneurosci.org as supplemental material), recorded Ca^{2+} fluorescence in giant MFs in response to 50 APs at 20 Hz (Fig. 3D). The resulting fluorescence plateau (Fig. 3D) suggested that the indicator was close to saturation (Jackson and Redman, 2003; Rusakov et al., 2005). To confirm that this is indeed the case, we compared 20 and 50 Hz trains of APs in seven giant MFs and found no significant difference in the maximum fluorescence signal F_{max} (difference, $7 \pm 5\%$; $n = 7$); similar experiments with a lower-affinity indicator Fluo-5F ($K_d \sim 1 \mu\text{M}$; trains of 75–150 APs) gave a qualitatively identical result (difference, $5 \pm 3\%$; $n = 7$) (Fig. 3E;

supplemental Fig. 7, available at www.jneurosci.org as supplemental material). The saturating trains of APs in Fluo-4 therefore gave average F_{max}/F and R/F ratios for Fluo-4 of 2.63 ± 0.31 and 6.8 ± 1.2 , respectively ($n = 14$). The estimates of $[\text{Ca}^{2+}]_{\text{rest}}$ in each individual giant MF were obtained by substituting individual F_{max}/F and R/F values in Equation 3; this gave an average $[\text{Ca}^{2+}]_{\text{rest}}$ of $116 \pm 20 \text{ nM}$ ($n = 14$) (Fig. 3F).

An alternative estimate of $[\text{Ca}^{2+}]_{\text{rest}}$ was obtained using another high-affinity Ca^{2+} indicator, Oregon Green BAPTA-1 (200 μM ; $K_d = 205 \text{ nM}$) for which $F_{\text{max}}/F_{\text{min}} \sim 6$ (Maravall et al., 2000; Jackson and Redman, 2003). With a similar protocol, these experiments gave an average F_{max}/F ratio of 2.15 ± 0.14 , predicting $[\text{Ca}^{2+}]_{\text{rest}}$ at $103 \pm 14 \text{ nM}$ ($n = 8$) (Fig. 3F). This was in good correspondence with the estimate based on Fluo-4.

Ca^{2+} kinetics at giant MFs

To quantify the kinetics of presynaptic Ca^{2+} transients triggered by APs, we routinely evoked five spikes at 20 Hz, a firing pattern compatible with that of individual granule cells *in vivo* (Henze et

al., 2002). The fluorescence response was analyzed using a single-compartment model of Ca^{2+} dynamics: this approach was relevant because the characteristic point-spread function of the imaging system was comparable with or larger than the characteristic cross section of giant MFBs (Fig. 4A–C) (see Materials and Methods). To account for the nonstationary kinetics during and shortly after rapid Ca^{2+} entry, we simulated the binding–unbinding reactions using an explicit finite-difference scheme (Sabatini and Regehr, 1998; Matveev et al., 2004; Rusakov et al., 2005).

The model included several independently estimated quantities: (1) $[\text{Ca}^{2+}]_{\text{rest}} \approx 110 \text{ nM}$; (2) a direct measure of the main endogenous buffer (calbindin-28K) concentration $[B]_{\text{tot}} = 160 \mu\text{M}$ (Muller et al., 2005), which is in line with an estimate derived from Ca^{2+} imaging (Jackson and Redman, 2003); (3) the Ca^{2+} entry half-duration of $\sim 0.5 \text{ ms}$ (Bischofberger et al., 2002); and (4) indicator concentration $[I]$ clamped by the whole-cell pipette (see supplemental Fig. 2, available at www.jneurosci.org as supplemental material). The remaining two free parameters were the total Ca^{2+} influx $\Delta[\text{Ca}^{2+}]_{\text{tot}}$ and the Ca^{2+} removal rate P . Adjusting these, however, had virtually independent effects on, respectively, the amplitude and the decay constant of the evoked Ca^{2+} -sensitive fluorescence transient: changing $\Delta[\text{Ca}^{2+}]_{\text{tot}}$ twofold produced a comparable change in the predicted $\Delta F/F$ amplitude but a $<5\%$ change in the decay constant; conversely, changing the Ca^{2+} removal constant P twofold produced a comparable change in the predicted decay constant but $<5\%$ alteration in the $\Delta F/F$ amplitude (supplemental Fig. 5, available at www.jneurosci.org as supplemental material). In these conditions, fitting the computed fluorescence kinetics to the experimental $\Delta F/F$ is relatively straightforward, as discussed previously (Rusakov et al., 2005). To cross-validate the unknowns of Ca^{2+}

dynamics under different buffer configurations, we conducted similar experiments at two different concentrations of Fluo-4 (200 and $50 \mu\text{M}$) and also with a lower-affinity indicator Fluo-5F. In all three cases, optimization with the two parameters gave a very good fit, yielding consistent estimates of $\Delta[\text{Ca}^{2+}]_{\text{tot}}$ and P (Fig. 4D–F). This consistency further argues that the previous estimates of the endogenous Ca^{2+} buffer concentration in the soma and proximal boutons (Jackson and Redman, 2003; Muller et al., 2005) are relevant for giant MFBs, as indeed expected from the long-term diffuse equilibration of soluble calbindin-28K. Together, the data thus predict $\Delta[\text{Ca}^{2+}]_{\text{tot}} = 51 \pm 2 \mu\text{M}$ and an average Ca^{2+} removal rate, $p = 0.37 \pm 0.03 \text{ ms}^{-1}$.

According to morphological observations, the volume of giant MFBs is in the region of $20\text{--}50 \mu\text{m}^3$ (Chicurel and Harris,

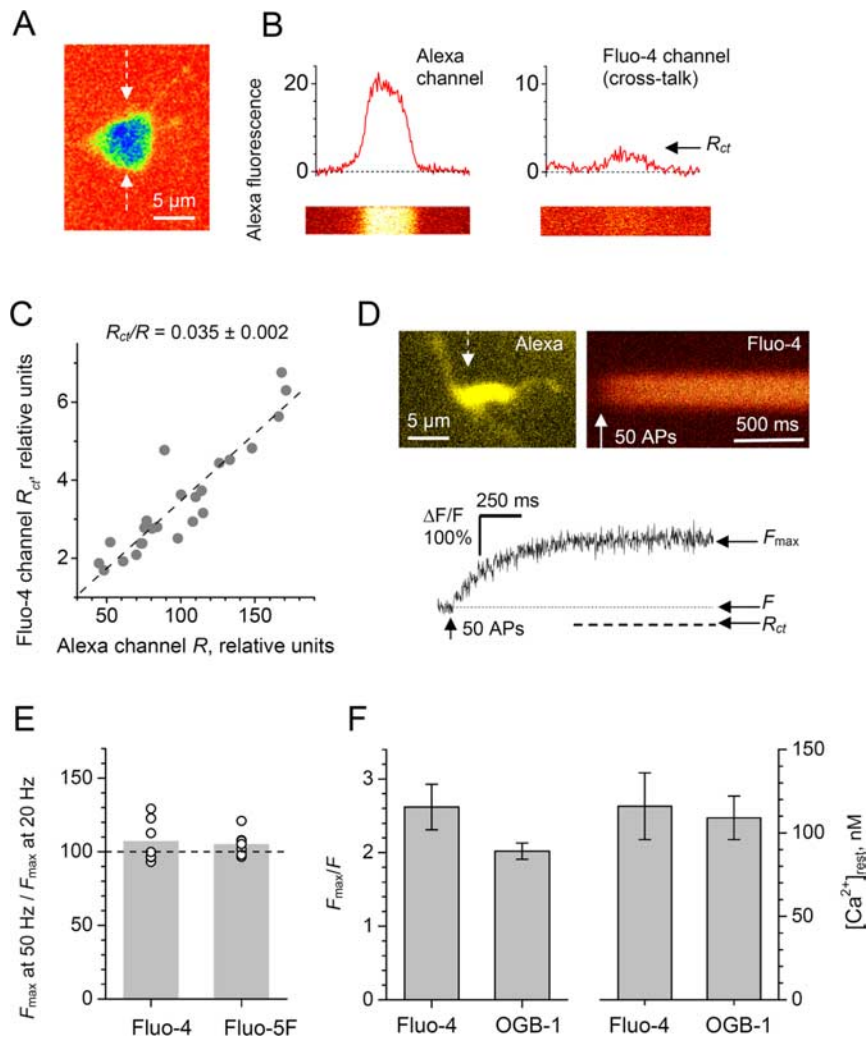


Figure 3. Estimation of the resting Ca^{2+} at giant MFBs using a cross-talk reference. **A**, An example of a giant MFB filled with $200 \mu\text{M}$ Alexa Fluor 594 only (no Ca^{2+} indicator); average of five frame scans. **B**, Line scans of the bouton shown in **A** (arrows) imaged in the Alexa Fluor 594 and Fluo-4 (cross-talk) channels, as indicated; arrow, cross-talk fluorescence signal of Alexa Fluor 594, R_{ct} . **C**, A summary of experiments shown in **A** and **B**. The Alexa Fluor 594 cross-talk signal recorded in the Fluo-4 channel (ordinate) is plotted against the Alexa Fluor 594 direct fluorescence signal (abscissa). The dotted line represents the best-fit linear regression, as indicated; background fluorescence is subtracted. **D**, A giant MFBs filled with $200 \mu\text{M}$ Fluo-4 and $20 \mu\text{M}$ Alexa Fluor 594 (left panel, Alexa Fluor 594 channel) and the corresponding line-scan $\Delta F/F$ signal (right panel and trace, Fluo-4 channel; recorded at 500 Hz) in response to 50 APs at 20 Hz ; the relationship between F_{max} , F , and R_{ct} is illustrated. **E**, Comparison of the plateau F_{max} levels obtained in response to 20 and 50 Hz trains of APs generated in the same giant MFB in experiments using Fluo-4 ($200 \mu\text{M}$; $K_d \sim 350 \text{ nM}$; $n = 7$) and Fluo-5F ($200 \mu\text{M}$; $K_d \sim 1 \mu\text{M}$; $n = 7$), as indicated. **F**, The average F_{max}/F ratios (left panel) and estimated $[\text{Ca}^{2+}]_{\text{rest}}$ (right panel) in giant MFBs obtained using fluorescent indicators Fluo-4 ($F_{\text{max}}/F = 2.62 \pm 0.31$; $[\text{Ca}^{2+}]_{\text{rest}} = 116 \pm 20 \text{ nM}$; $n = 15$) and OGB-1 ($F_{\text{max}}/F = 2.15 \pm 0.14$; $[\text{Ca}^{2+}]_{\text{rest}} = 103 \pm 14 \text{ nM}$; $n = 8$), as indicated. Error bars indicate SEM.

1992; Acsady et al., 1998), or $2\text{--}5 \times 10^{-14} \text{ L}$. In electron micrographs, synaptic vesicles and mitochondria appear to occupy $\sim 50\%$ of the giant MFB profile (Fig. 4B,C); this is likely to scale down twofold the volume available to Ca^{2+} ions. The $\sim 50 \mu\text{M}$ step concentration increase (3×10^{19} ions/L) would then correspond to $3\text{--}8 \times 10^5 \text{ Ca}^{2+}$ ions per bouton. This is in excellent agreement with electrophysiological observations showing that $3.7 \times 10^5 \text{ Ca}^{2+}$ ions flow into a patched giant MFB following an AP (Bischofberger et al., 2002). The estimated Ca^{2+} dynamics is also in correspondence with the unchanged Ca^{2+} entry during short 20 Hz AP trains (Geiger and Jonas, 2000). Together, these data provide quantitative insights into the presynaptic Ca^{2+} kinetics in the absence of exogenous buffering imposed by Ca^{2+} indicators (see Fig. 6) (see Discussion).

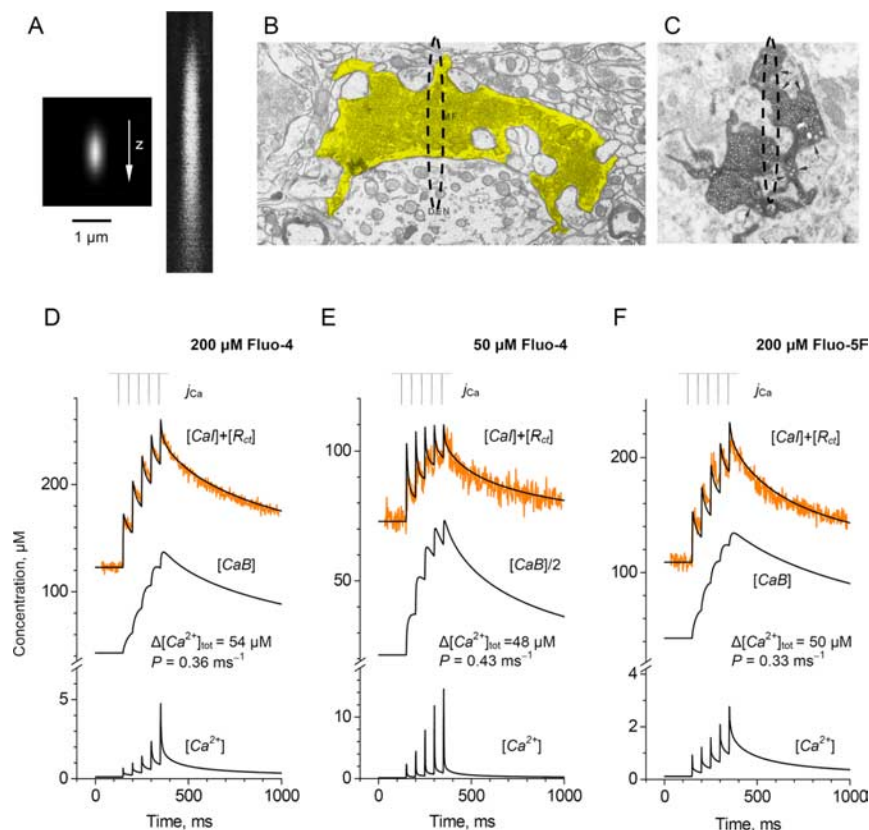


Figure 4. Action potential-evoked Ca^{2+} transients in giant MFBs in the CA3 region. **A**, The two-photon excitation PSF evaluated for the optical settings used. Left panel, A vertical central section of the theoretical (lower-limit) diffraction-limited excitation probability profile (see Materials and Methods). Right panel, A vertical central section of the 2P PSF measured using 0.17 nm fluorescence beads and a three-dimensional reconstruction of 42 consecutive optical sections 0.25 μm apart. Linear brightness scale, 0–1; scale bar applies to **A–C**. **B**, **C**, Characteristic electron micrographs of giant MF bouton profiles, modified from Chicurel and Harris (1992) (**B**, yellow shade) and from Acsády et al. (1998) (**C**, dark staining indicates rabbit anti-substance P immunoreaction identifying a single presynaptic axon). Comparing these to the PSF (dashed ellipse) suggests that optical recordings normally deal with fluorescence volume-averaged across the MFB lumen. **D**, **E**, **F**, Fluorescence recordings and computed kinetic reaction components at three Ca^{2+} indicator settings, as indicated. The top trace inset illustrates five simulated AP-evoked pulses of Ca^{2+} influx; relative scale. Orange traces, Experimental recordings: the average fluorescence time course (global mean for $n = 18$, 5, and 5 cells in **D**, **E**, and **F**, respectively). The black lines represent simulated data: the best-fit predictions for the recorded fluorescence $[\text{Ca}] + [\text{R}_{\text{cl}}]$, bound Ca^{2+} buffer $[\text{CaB}]$, and free Ca^{2+} $[\text{Ca}^{2+}]$. Best-fit values for total Ca^{2+} entry $\Delta[\text{Ca}^{2+}]_{\text{tot}}$ and removal rate P are shown.

Internal Ca^{2+} stores and presynaptic Ca^{2+} signaling

The role of presynaptic Ca^{2+} stores at MF synapses remains controversial (Carter et al., 2002; Liang et al., 2002; Lauri et al., 2003; Breustedt and Schmitz, 2004). To address this, we imaged giant MFBs loaded with either Fluo-4 or Fluo-5F (200 μM) (Fig. 5*A*, *B*) and, once the Ca^{2+} responses were stable (supplemental Fig. 2, available at www.jneurosci.org as supplemental material), applied either ryanodine (20–60 μM) or thapsigargin (1 μM). These blockers interfere with Ca^{2+} -induced ryanodine receptor-dependent Ca^{2+} release or with the endoplasmic reticulum Ca^{2+} -ATPase (Ca^{2+} pump), respectively. Because Ca^{2+} stores might not respond to a single AP (Lauri et al., 2003), we routinely evoked five or more APs at 20 Hz and measured the integrated $\Delta F/F$ signal over a 500 ms window from the first response onset.

Although ryanodine and thapsigargin interfere with different mechanisms of internal Ca^{2+} storage, the longer-term consequence is thought to be the blockade/depletion of endoplasmic reticulum Ca^{2+} stores (Verkhratsky, 2005). Indeed, both ryanodine and thapsigargin produced a small yet significant increase in the resting fluorescence F ($11 \pm 3\%$, $n = 8$, $p < 0.02$; and $12 \pm$

3%, $n = 5$, $p < 0.02$, respectively) and a decrease in $\Delta F/F$ ($18 \pm 6\%$, $n = 8$, $p < 0.02$; and $8 \pm 7\%$, $n = 5$, NS, respectively), recorded in experiments with the high-affinity Fluo-4 (Fig. 5*D–F*). In contrast, ryanodine application in experiments with the lower-affinity Fluo-5F produced only insignificant increases in F , yet it decreased $\Delta F/F$ robustly ($17 \pm 4\%$, $p < 0.004$; integrated over six APs) (Fig. 5*G–I*). In both cases, the significant changes exceeded at least threefold the experimental fluctuations of F and $\Delta F/F$ documented in baseline conditions on a similar time-scale (supplemental Fig. 2*B*, *C*, available at www.jneurosci.org as supplemental material).

These results are consistent with an elevation in the resting Ca^{2+} concentration, $[\text{Ca}^{2+}]_{\text{rest}}$: the higher affinity Fluo-4 is more sensitive than Fluo-5F to changes in $[\text{Ca}^{2+}]_{\text{rest}}$, yet it saturates to a greater degree and therefore is less sensitive to changes in $\Delta F/F$. According to Equation 3, in baseline conditions of Fluo-4 fluorescence, a $\sim 12\%$ increase in F corresponds to an increase in $[\text{Ca}^{2+}]_{\text{rest}}$ of 40–50 nM. In the case of lower-affinity Fluo-5F, however, the same increase in $[\text{Ca}^{2+}]_{\text{rest}}$ should produce a much smaller elevation of F , which is fully consistent with our observations. In line with the buffering role of Ca^{2+} stores, their blockade also slowed down the decay of the $\Delta F/F$ signal following five or more APs: by $21 \pm 8\%$ in Fluo-4 experiments (the apparent decay time constant changed from 730 ± 111 to 856 ± 110 ms; $n = 10$; $p < 0.03$) and by $34 \pm 12\%$ in Fluo-5F experiments (time constant changed from 1106 ± 121 to 1533 ± 295 ms; $n = 65$; $p < 0.004$); the fluorescent decay in these

multi-AP recordings was substantially slower than that following a single AP (Fig. 2), partly because of the indicator saturation.

Discussion

In this study, we have evaluated the main determinants of Ca^{2+} signals generated in individual giant MFBs by electrical activity in a single granule cell. Somatic voltage, which affects Ca^{2+} responses in proximal axonal compartments, does not influence rapid Ca^{2+} transients in giant MFBs. We find that Ca^{2+} stores take part in maintaining the resting concentration of presynaptic Ca^{2+} , a mechanism which has not previously been reported in cortical synapses. Rapid Ca^{2+} release from internal stores also contributes to Ca^{2+} transients in giant MFBs (this could be masked in multiple MF recordings, at least in part, if other MF compartments were insensitive to Ca^{2+} store blockade). The data provide a basis for deciphering the kinetics of free Ca^{2+} at giant MFBs, a key to presynaptic mechanisms of use-dependent plasticity at the MF–CA3 pyramidal cell synapse, as discussed below.

Electrotonic control of presynaptic Ca^{2+} entry

The regulatory role of presynaptic ionotropic receptors in neurotransmitter release has attracted much interest (Engelman and MacDermott, 2004). However, to what extent presynaptic electrotonic influences spread along the terminal remains poorly understood. Although the granule cell somatic voltage affects Ca^{2+} kinetics at MF axonal boutons in the hilus (Ruiz et al., 2003), we detected no such influence at giant MFBs in CA3. This was consistent with the estimated electrotonic length constant of Ca^{2+} entry control in MFs, $\lambda = 150\text{--}200\ \mu\text{m}$, also agreeing with the lack of somatic voltage control over MF excitability in stratum lucidum (Schmitz et al., 2000). However, very recent observations of presynaptic EPSCs in giant MFBs have proposed an MF electrotonic length constant of $\sim 450\ \mu\text{m}$ (Alle and Geiger, 2006). The most parsimonious explanation for the difference is that AP-evoked Ca^{2+} entry is not sensitive to small changes in the local membrane potential. Indeed, somatic voltage has no effect on Ca^{2+} currents in giant MFBs (Alle and Geiger, 2006). In any case, the value of λ suggests that the Ca^{2+} -dependent release machinery acting at synapses between granule cells and interneurons or mossy cells in the hilus could be influenced by the resting somatic membrane voltage. Conversely, presynaptic ionotropic action could propagate between neighboring giant MFBs occurring 100–200 μm apart (Acsady et al., 1998).

At the calyx of Held, moderate presynaptic depolarization increases the resting Ca^{2+} concentration, thus augmenting the release probability (Turecek and Trussell, 2001; Awatramani et al., 2005). The depolarization-induced elevation of resting Ca^{2+} was also reported in proximal MFBs (Ruiz et al., 2003). If similar phenomena occur locally in giant MFBs, an increase in the postsynaptic responses could follow (Alle and Geiger, 2006). This might reconcile the facilitatory effect of low kainate concentration on MF transmission (Schmitz et al., 2001) with the depolarizing action of kainate receptors. Furthermore, presynaptic depolarization could initiate AP broadening (Geiger and Jonas, 2000), thus boosting Ca^{2+} entry and the release probability further.

Kinetics of free Ca^{2+} and short-term synaptic facilitation

We have used several Ca^{2+} indicator configurations to estimate and cross-validate Ca^{2+} kinetics at giant MFBs. Although our experiments rely on fluorophores that directly interfere with Ca^{2+} buffering, the resulting kinetic model allows evaluation of the free Ca^{2+} kinetics in the absence of exogenous buffers (Fig. 6A). The data predict substantial use-dependent facilitation of

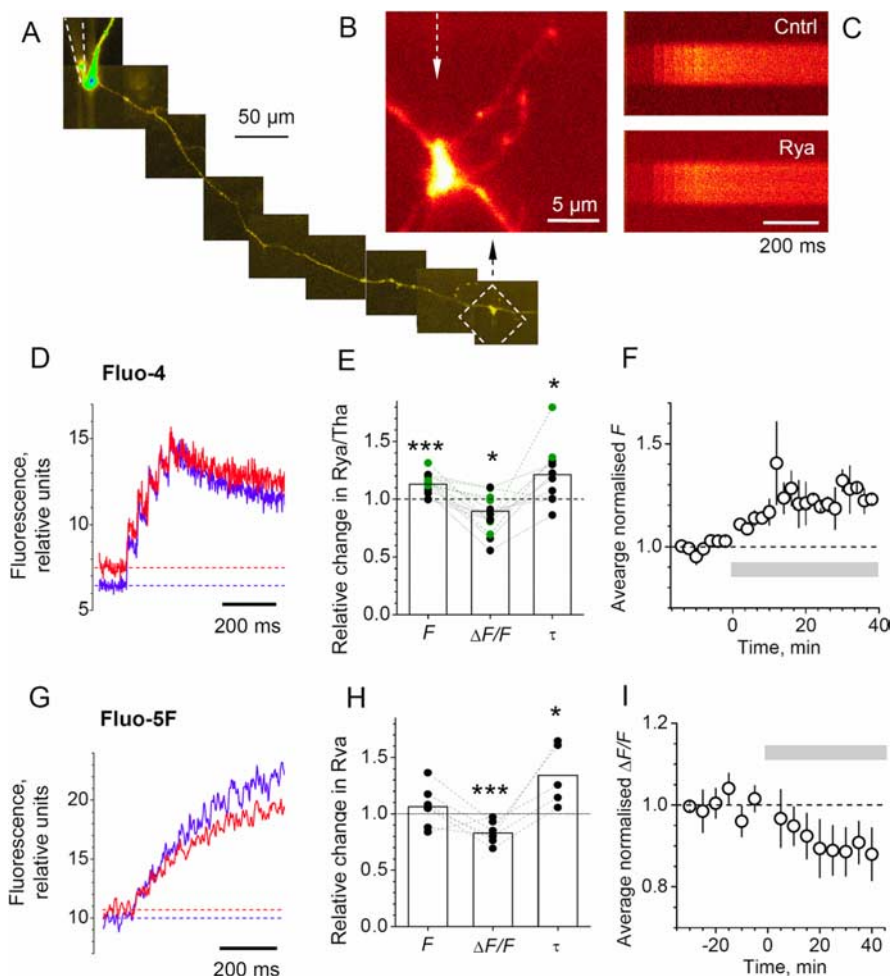


Figure 5. Ca^{2+} store depletion increases resting Ca^{2+} but decreases Ca^{2+} transients. **A–C**, Single-cell example. A reconstructed granule cell axon (**A**); dashed square, the giant MFB of interest enlarged in **B** (Alexa Fluor 594 channel). Line scans in **C** (Fluo-4 channel) show recordings from the bouton in **B**, an average of seven traces. Cntrl, Control; Rya, ~ 10 min after application of 50 μM ryanodine. **D**, Effect of Ca^{2+} store blockers ryanodine ($n = 8$) or thapsigargin ($n = 5$) on Ca^{2+} signaling in experiments with 200 μM Fluo-4 (applies to **D–F**). The average fluorescence kinetics in response to five APs (global mean; $n = 13$) in control (blue) and test (red) conditions. **E**, Relative changes in baseline signal F , $\Delta F/F$ (integrated over five pulses), and fluorescence decay time τ (single exponent) after application of ryanodine ($n = 8$; black circles) or thapsigargin ($n = 5$; green circles) in individual cells. The overall changes are as follows ($n = 13$; see Results for separate statistics on ryanodine and thapsigargin): F , $12 \pm 2\%$ ($***p < 0.001$); $\Delta F/F$, $-13 \pm 5\%$ ($*p < 0.03$); τ , $21 \pm 8\%$ ($*p < 0.03$); the dashed lines connect data points from the same MFB. **F**, The time course of changes in the resting F (normalized values) after ryanodine application (gray segment) in the experiments shown in **D** and **E**. The circles represent global mean; error bars indicate SEM. **G, H**, Experiments using 200 μM Fluo-5F; notations are the same as in **D** and **E** for ryanodine application; average changes are as follows: F , $6 \pm 6\%$ ($n = 7$; NS); $\Delta F/F$, $-17 \pm 4\%$ ($n = 7$; $***p < 0.004$); τ , $34 \pm 12\%$ ($n = 5$; $*p < 0.04$). **I**, The time course of changes in the resting F (normalized values) after drug application (gray segment) in experiments shown in **G** and **H**. The circles represent global mean; error bars indicate SEM.

both rapid Ca^{2+} transients and residual Ca^{2+} rises, with the latter extending beyond 500 ms postpulse (Fig. 6A, gray line). However, the volume-integrated kinetics could underrepresent concentration microdomains near Ca^{2+} entry sites, thus underestimating local buffer saturation and hence overestimating use-dependent facilitation of local free Ca^{2+} (Meinrenken et al., 2003). Nonetheless, even modest facilitation would increase the release probability substantially if neurotransmitter release at MFBs depended on Ca^{2+} in a highly supralinear manner, as reported in the calyx of Held (Schneppenburger and Neher, 2000). This is, however, not the case in giant MFBs: increasing presynaptic Ca^{2+} transient through either AP broadening, elevation in external Ca^{2+} , or changed buffering conditions enhances MF–CA3 pyramidal cell transmission with the less than second power

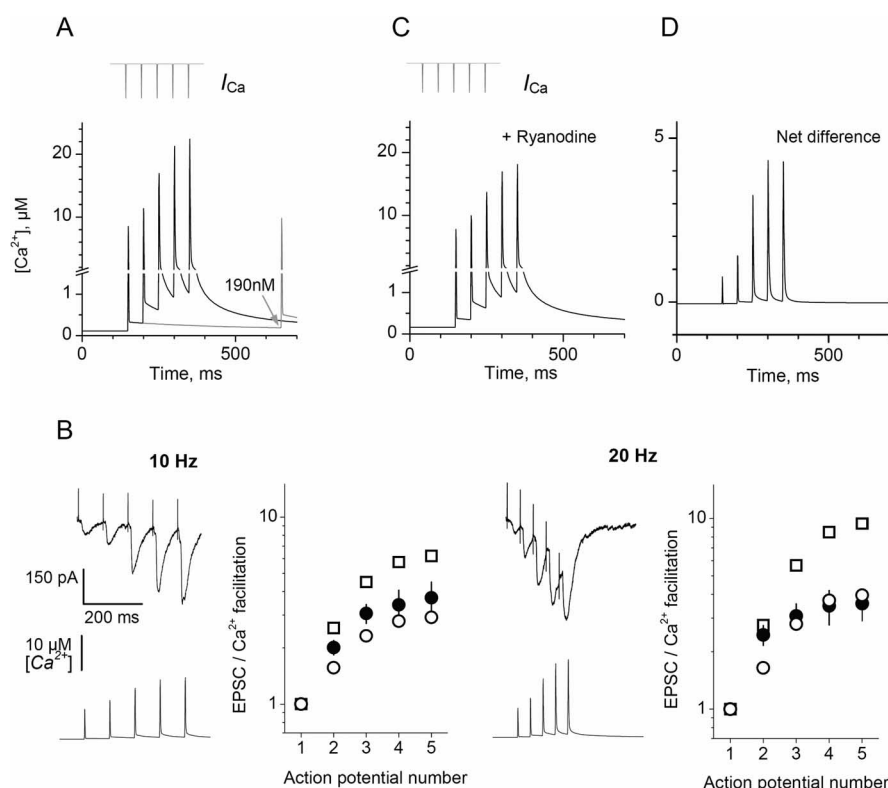


Figure 6. Kinetics of free Ca^{2+} and synaptic facilitation at MF–CA3 pyramidal cell synapses. **A**, According to the predicted kinetics, Ca^{2+} entry driven by five APs at 20 Hz (inset) corresponds to a progressive increase in peak and residual free $[\text{Ca}^{2+}]$; two spikes 500 ms apart (gray line) show modest facilitation of the peak $[\text{Ca}^{2+}]$ value (15%) and a more substantial increase of the integrated $[\text{Ca}^{2+}]$ spike (34%; averaged over 4 ms during the AP) and residual $[\text{Ca}^{2+}]$ elevation (73%; gray arrow). **B**, Insets show a single-cell example of recorded responses (top trace) and the corresponding calculated time course of free presynaptic $[\text{Ca}^{2+}]$ (bottom trace) at two stimulation frequencies, as indicated. Plots compare the use-dependent facilitation of the computed rapid spikes of free Ca^{2+} (average $[\text{Ca}^{2+}]$ over 4 ms during an AP; open circles), the computed residual prepulse $[\text{Ca}^{2+}]$ (open squares), and the average experimental EPSC amplitude (filled circles) in CA3 pyramidal cells in response to five APs ($n = 5$ cells). All values are normalized with respect to the first response. **C**, Same as in **A** but the blockade of Ca^{2+} -induced Ca^{2+} release from stores is mimicked as a reduction in evoked Ca^{2+} entry by 20% and an increase in resting Ca^{2+} by 40% (see Results). **D**, The difference between **A** and **C** illustrating net contribution of Ca^{2+} store releases to free Ca^{2+} transients.

relationship (Regehr et al., 1994; Geiger and Jonas, 2000; Blatow et al., 2003; Mori-Kawakami et al., 2003). The question therefore arises whether the kinetics of free presynaptic Ca^{2+} evaluated here could explain short-term synaptic facilitation at these synapses.

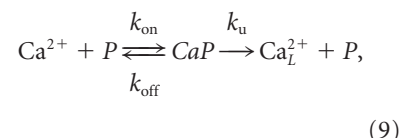
To address this, we calculated use-dependent increases of residual $[\text{Ca}^{2+}]$ and rapid $[\text{Ca}^{2+}]$ transients (average $[\text{Ca}^{2+}]$ elevation over 4 ms during an AP) in giant MFBs and compared them with the average facilitation of EPSCs evoked in CA3 pyramidal cells by short trains of APs at 10 and 20 Hz (elicited by extracellular stimuli in dentate gyrus) (Fig. 6B). The comparison suggests that, in conditions of our experiments, synaptic facilitation follows more closely rapid $[\text{Ca}^{2+}]$ transients than residual $[\text{Ca}^{2+}]$ rises (with an exception of the second pulse). Although these data suggest a causal link between facilitation of presynaptic Ca^{2+} signals and postsynaptic responses, it would be important to establish how the presynaptic Ca^{2+} kinetics reflects synaptic adaptation to different firing patterns (Zucker and Regehr, 2002).

A role for Ca^{2+} stores

We found that blockade of internal Ca^{2+} stores in giant MFBs elevates resting Ca^{2+} by $\sim 40\%$. Although this phenomenon has not previously been reported in cortical synapses, it is not sur-

prising: the Ca^{2+} concentration inside endoplasmic reticulum stores is critical for cytosolic Ca^{2+} homeostasis (Verkhratsky, 2005). Indeed, Ca^{2+} leakage from the stores is negatively coupled with Ca^{2+} uptake, producing a kinetic equilibrium (Solovyova et al., 2002), which is likely to reflect the resting Ca^{2+} level. By taking Ca^{2+} stores out of the equilibrium, ryanodine blockade should reduce the Ca^{2+} removal capacity of giant MFBs, thus elevating resting Ca^{2+} concentration. The present data allow us to evaluate this quantitatively.

Ca^{2+} removal depends primarily on the two families of Ca^{2+} pumps, the plasma membrane Ca^{2+} -ATPase and the sarco/endoplasmic reticulum Ca^{2+} -ATPase; mitochondria and a low-affinity $\text{Na}^{+}/\text{Ca}^{2+}$ exchanger also contribute to Ca^{2+} removal, albeit on a slower timescale (for review, see Parekh, 2003; Mata and Sepulveda, 2005; Verkhratsky, 2005). Because pumps operate through binding and translocation, Ca^{2+} uptake kinetics could be generally represented by the following two-stage reaction:



where P and Ca_i^{2+} denote pumps and intralumen Ca^{2+} , respectively, CaP stands for the Ca-bound pump complex, and k_{on} , k_{off} , and k_u stand for the average rate constants of Ca^{2+} binding, unbinding, and translocation (coupled with the reappearance of available pumps P), respectively. These reactions (Eq. 9) evoke the following simple kinetic equations:

$$\frac{\partial [\text{Ca}^{2+}]}{\partial t} = L_{\text{Ca}} - k_{\text{on}}[\text{Ca}^{2+}][P] + k_{\text{off}}[\text{CaP}] \quad (10a)$$

$$\frac{\partial [\text{CaP}]}{\partial t} = k_{\text{on}}[\text{Ca}^{2+}][P] - (k_{\text{off}} + k_u)[\text{CaP}], \quad (10b)$$

with the mass conservation law

$$[P] + [\text{CaP}] = [P]_{\text{tot}}, \quad (10c)$$

where brackets denote concentration, L_{Ca} is the rate of overall Ca^{2+} leakage into the cytosol, and $[P]_{\text{tot}}$ is the total amount of available pumps. In the steady-state case (time derivatives zeroed), Equations 10a, 10b, and 10c reflect equilibration between uptake and leakage as follows:

$$k_u[\text{CaP}] = L_{\text{Ca}}. \quad (11a)$$

The equilibrium corresponds to the resting Ca^{2+} level, $[\text{Ca}^{2+}]_{\text{rest}}$, evoking the following relationship:

$$[P]_{\text{tot}} = \frac{L_{\text{Ca}}}{k_u} \left(1 + \frac{k_{\text{off}} + k_u}{k_{\text{on}}[\text{Ca}^{2+}]_{\text{rest}}} \right). \quad (11b)$$

Direct monitoring of Ca^{2+} store uptake in dorsal root ganglion neurons and in pancreatic acinar cells has indicated that the maximum uptake rate (after caffeine-induced Ca^{2+} release) is approximately four times greater than the resting uptake rate (Mogami et al., 1998; Solovyova et al., 2002). Because the maximum uptake is likely to reflect Ca^{2+} pump saturation, which implies $[\text{CaP}] \rightarrow [P]_{\text{tot}}$, Equation 11a predicts the relationship $k_u[P]_{\text{tot}} \approx 4L_{\text{Ca}}$. Substituted in Equation 11b, this gives the following:

$$\frac{k_{\text{off}} + k_u}{k_{\text{on}}[\text{Ca}^{2+}]_{\text{rest}}} \approx 3. \quad (12a)$$

When Ca^{2+} stores are blocked, this should reduce the concentration of available pumps to $[P]_{\text{tot}}^*$, thus elevating $[\text{Ca}^{2+}]_{\text{rest}}$ by ~40% (see Results). Equations 12a and 11b recast in terms of the elevated Ca^{2+} level $[\text{Ca}^{2+}]_{\text{rest}}^* = 1.4[\text{Ca}^{2+}]_{\text{rest}}$ and $[P]_{\text{tot}}^*$, thus yield $k_u[P]_{\text{tot}}^* \approx 3.1L_{\text{Ca}}$, or $[P]_{\text{tot}}^* \approx 0.78[P]_{\text{tot}}$. Store blockade, therefore, removes ~22% of the buffering/uptake capacity that maintains the low resting Ca^{2+} concentration. This value is consistent with a ryanodine-induced prolongation of the $\Delta F/F$ decay, which depends mainly on Ca^{2+} removal.

We also find that blockade of Ca^{2+} stores reduces by up to 20% the Ca^{2+} transients evoked in giant MFBs by a short train of APs. This is consistent with the progressive decrease of EPSCs recorded in CA3 pyramidal cells after Ca^{2+} store blockade (Lauri et al., 2003). Incorporating a 20% reduction of Ca^{2+} entry and a 40% increase in resting Ca^{2+} concentration into the indicator-free model (Fig. 6A) predicts the free Ca^{2+} kinetics depicted in Figure 6C. Interestingly, the difference between the two cases (Fig. 6A, C) suggests little impact of stores on the first two Ca^{2+} transients (Fig. 6D). This is because the reduction in Ca^{2+} entry is compensated for by the reduced buffering capacity (attributable to the elevated resting Ca^{2+}). The phenomenon might explain, at least partly, why blockade of Ca^{2+} stores has little influence on single or paired synaptic responses (Carter et al., 2002; Liang et al., 2002; Lauri et al., 2003). Reduction in Ca^{2+} buffering capacity through elevation of resting Ca^{2+} could also contribute to the release probability increase at the calyx of Held after presynaptic depolarization (Turecek and Trussell, 2001; Awatramani et al., 2005).

Although this mechanism acts at the giant MFBs representing synapses on CA3 pyramidal cells, the main synaptic target of MFs are interneurons (Acsady et al., 1998; Lawrence and McBain, 2003; Mori et al., 2004). The MF–interneuron synapses in CA3 are formed either by filopodial extensions of giant MFBs or by en passant boutons (Acsady et al., 1998). These presynaptic specializations show clear AP-evoked Ca^{2+} signals that are insensitive to ryanodine (our unpublished observations), whereas the corresponding synapses exhibit use-dependent plasticity distinct from that at MF–CA3 pyramidal cell synapses (Toth et al., 2000; Pelkey et al., 2005). Whether this functional diversity of MF synapses in CA3 could explain why Ca^{2+} store blockade has little effect on Ca^{2+} -dependent fluorescence recorded in bulk-loaded MFs (Carter et al., 2002; Breustedt and Schmitz, 2004) remains to be established.

References

- Acsady L, Kamondi A, Sik A, Freund T, Buzsaki G (1998) GABAergic cells are the major postsynaptic targets of mossy fibers in the rat hippocampus. *J Neurosci* 18:3386–3403.
- Alle H, Geiger JD (2006) Combined analog and action potential coding in hippocampal mossy fibers. *Science* 311:1290–1293.
- Amaral DG, Ishizuka N, Claiborne B (1990) Neurons, numbers and the hippocampal network. *Prog Brain Res* 83:1–11.
- Awatramani GB, Price GD, Trussell LO (2005) Modulation of transmitter release by presynaptic resting potential and background calcium levels. *Neuron* 48:109–121.
- Berggard T, Miron S, Onnerfjord P, Thulin E, Akerfeldt KS, Enghild JJ, Akke M, Linse S (2002) Calbindin D28k exhibits properties characteristic of a Ca^{2+} sensor. *J Biol Chem* 277:16662–16672.
- Bischofberger J, Geiger JR, Jonas P (2002) Timing and efficacy of Ca^{2+} channel activation in hippocampal mossy fiber boutons. *J Neurosci* 22:10593–10602.
- Blatow M, Caputi A, Burnashev N, Monyer H, Rozov A (2003) Ca^{2+} buffer saturation underlies paired pulse facilitation in calbindin-D28k-containing terminals. *Neuron* 38:79–88.
- Breustedt J, Schmitz D (2004) Assessing the role of GLUK5 and GLUK6 at hippocampal mossy fiber synapses. *J Neurosci* 24:10093–10098.
- Carter AG, Vogt KE, Foster KA, Regehr WG (2002) Assessing the role of calcium-induced calcium release in short-term presynaptic plasticity at excitatory central synapses. *J Neurosci* 22:21–28.
- Chicurel ME, Harris KM (1992) Three-dimensional analysis of the structure and composition of CA3 branched dendritic spines and their synaptic relationships with mossy fiber boutons in the rat hippocampus. *J Comp Neurol* 325:169–182.
- Claiborne BJ, Amaral DG, Cowan WM (1990) Quantitative, three-dimensional analysis of granule cell dendrites in the rat dentate gyrus. *J Comp Neurol* 302:206–219.
- Contractor A, Swanson G, Heinemann SF (2001) Kainate receptors are involved in short- and long-term plasticity at mossy fiber synapses in the hippocampus. *Neuron* 29:209–216.
- Engel D, Jonas P (2005) Presynaptic action potential amplification by voltage-gated Na^{+} channels in hippocampal mossy fiber boutons. *Neuron* 45:405–417.
- Engelman HS, MacDermott AB (2004) Presynaptic ionotropic receptors and control of transmitter release. *Nat Rev Neurosci* 5:135–145.
- Gee KR, Brown KA, Chen WN, Bishop-Stewart J, Gray D, Johnson I (2000) Chemical and physiological characterization of fluo-4 Ca^{2+} -indicator dyes. *Cell Calcium* 27:97–106.
- Geiger JRP, Jonas P (2000) Dynamic control of presynaptic Ca^{2+} inflow by fast-inactivating K^{+} channels in hippocampal mossy fiber boutons. *Neuron* 28:927–939.
- Griffith WH (1990) Voltage-clamp analysis of posttetanic potentiation of the mossy fiber to CA3 synapse in hippocampus. *J Neurophysiol* 63:491–501.
- Helmchen F, Borst JG, Sakmann B (1997) Calcium dynamics associated with a single action potential in a CNS presynaptic terminal. *Biophys J* 72:1458–1471.
- Henze DA, Wittner L, Buzsaki G (2002) Single granule cells reliably discharge targets in the hippocampal CA3 network in vivo. *Nat Neurosci* 5:790–795.
- Holcman D, Korkotian E, Segal M (2005) Calcium dynamics in dendritic spines, modeling and experiments. *Cell Calcium* 37:467–475.
- Jackson MB (1992) Cable analysis with the whole-cell patch clamp. Theory and experiment. *Biophys J* 61:756–766.
- Jackson MB, Redman SJ (2003) Calcium dynamics, buffering, and buffer saturation in the boutons of dentate granule-cell axons in the hilus. *J Neurosci* 23:1612–1621.
- Kamiya H, Ozawa S, Manabe T (2002) Kainate receptor-dependent short-term plasticity of presynaptic Ca^{2+} influx at the hippocampal mossy fiber synapses. *J Neurosci* 22:9237–9243.
- Koester HJ, Johnston D (2005) Target cell-dependent normalization of transmitter release at neocortical synapses. *Science* 308:863–866.
- Koester HJ, Sakmann B (2000) Calcium dynamics associated with action potentials in single nerve terminals of pyramidal cells in layer 2/3 of the young rat neocortex. *J Physiol (Lond)* 529:625–646.
- Lauri SE, Bortolotto ZA, Bleakman D, Ornstein PL, Lodge D, Isaac JTR,

- Collingridge GL (2001) A critical role of a facilitatory presynaptic kainate receptor in mossy fiber LTP. *Neuron* 32:697–709.
- Lauri SE, Bortolotto ZA, Nistico R, Bleakman D, Ornstein PL, Lodge D, Isaac JT, Collingridge GL (2003) A role for Ca^{2+} stores in kainate receptor-dependent synaptic facilitation and LTP at mossy fiber synapses in the hippocampus. *Neuron* 39:327–341.
- Lawrence JJ, McBain CJ (2003) Interneuron diversity series: containing the detonation—feedforward inhibition in the CA3 hippocampus. *Trends Neurosci* 26:631–640.
- Liang Y, Yuan LL, Johnston D, Gray R (2002) Calcium signaling at single mossy fiber presynaptic terminals in the rat hippocampus. *J Neurophysiol* 87:1132–1137.
- Maravall M, Mainen ZF, Sabatini BL, Svoboda K (2000) Estimating intracellular calcium concentrations and buffering without wavelength ratioing. *Biophys J* 78:2655–2667.
- Mata AM, Sepulveda MR (2005) Calcium pumps in the central nervous system. *Brain Res Brain Res Rev* 49:398–405.
- Matveev V, Zucker RS, Sherman A (2004) Facilitation through buffer saturation: constraints on endogenous buffering properties. *Biophys J* 86:2691–2709.
- Meinrenken CJ, Borst JGG, Sakmann B (2003) Local routes revisited: the space and time dependence of the Ca^{2+} signal for phasic transmitter release at the rat calyx of Held. *J Physiol (Lond)* 547:665–689.
- Mogami H, Tepikin AV, Petersen OH (1998) Termination of cytosolic Ca^{2+} signals: Ca^{2+} reuptake into intracellular stores is regulated by the free Ca^{2+} concentration in the store lumen. *EMBO J* 17:435–442.
- Mori M, Abegg MH, Gähwiler BH, Gerber U (2004) A frequency-dependent switch from inhibition to excitation in a hippocampal unitary circuit. *Nature* 431:453–456.
- Mori-Kawakami F, Kobayashi K, Takahashi T (2003) Developmental decrease in synaptic facilitation at the mouse hippocampal mossy fibre synapse. *J Physiol (Lond)* 553:37–48.
- Muller A, Kukley M, Stausberg P, Beck H, Muller W, Dietrich D (2005) Endogenous Ca^{2+} buffer concentration and Ca^{2+} microdomains in hippocampal neurons. *J Neurosci* 25:558–565.
- Nagerl UV, Novo D, Mody I, Vergara JL (2000) Binding kinetics of calbindin- D_{28k} determined by flash photolysis of caged Ca^{2+} . *Biophys J* 79:3009–3018.
- Naraghi M (1997) T-jump study of calcium binding kinetics of calcium chelators. *Cell Calcium* 22:255–268.
- Neher E (1998) Usefulness and limitations of linear approximations to the understanding of Ca^{++} signals. *Cell Calcium* 24:345–357.
- Oertner TG, Sabatini BL, Nimchinsky EA, Svoboda K (2002) Facilitation at single synapses probed with optical quantal analysis. *Nat Neurosci* 5:657–664.
- Parekh AB (2003) Store-operated Ca^{2+} entry: dynamic interplay between endoplasmic reticulum, mitochondria and plasma membrane. *J Physiol (Lond)* 547:333–348.
- Pelkey KA, Lavezzi G, Racca C, Roche KW, McBain CJ (2005) mGluR7 is a metaplastic switch controlling bidirectional plasticity of feedforward inhibition. *Neuron* 46:89–102.
- Regehr WG, Delaney KR, Tank DW (1994) The role of presynaptic calcium in short-term enhancement at the hippocampal mossy fiber synapse. *J Neurosci* 14:523–537.
- Rozov A, Burnashev N, Sakmann B, Neher E (2001) Transmitter release modulation by intracellular Ca^{2+} buffers in facilitating and depressing nerve terminals of pyramidal cells in layer 2/3 of the rat neocortex indicates a target cell-specific difference in presynaptic calcium dynamics. *J Physiol (Lond)* 531:807–826.
- Ruiz A, Fabian-Fine R, Scott R, Walker MC, Rusakov DA, Kullmann DM (2003) GABAA receptors at hippocampal mossy fibers. *Neuron* 39:961–973.
- Rusakov DA, Fine A (2003) Extracellular Ca^{2+} depletion contributes to fast activity-dependent modulation of synaptic transmission in the brain. *Neuron* 37:287–297.
- Rusakov DA, Wuerz A, Kullmann DM (2004) Heterogeneity and specificity of presynaptic Ca^{2+} current modulation by mGluRs at individual hippocampal synapses. *Cereb Cortex* 14:748–758.
- Rusakov DA, Saitow F, Lehre KP, Konishi S (2005) Modulation of presynaptic Ca^{2+} entry by AMPA receptors at individual GABAergic synapses in the cerebellum. *J Neurosci* 25:4930–4940.
- Sabatini BL, Regehr WG (1998) Optical measurement of presynaptic calcium currents. *Biophys J* 74:1549–1563.
- Sabatini BL, Oertner TG, Svoboda K (2002) The life cycle of Ca^{2+} ions in dendritic spines. *Neuron* 33:439–452.
- Schmitz D, Frerking M, Nicoll RA (2000) Synaptic activation of presynaptic kainate receptors on hippocampal mossy fiber synapses. *Neuron* 27:327–338.
- Schmitz D, Mellor J, Nicoll RA (2001) Presynaptic kainate receptor mediation of frequency facilitation at hippocampal mossy fiber synapses. *Science* 291:1972–1976.
- Schneggenburger R, Neher E (2000) Intracellular calcium dependence of transmitter release rates at a fast central synapse. *Nature* 406:889–893.
- Schneggenburger R, Sakaba T, Neher E (2002) Vesicle pools and short-term synaptic depression: lessons from a large synapse. *Trends Neurosci* 25:206–212.
- Scimemi A, Fine A, Kullmann DM, Rusakov DA (2004) NR2B-containing receptors mediate cross talk among hippocampal synapses. *J Neurosci* 24:4767–4777.
- Solovyova N, Veselovsky N, Toescu EC, Verkhratsky A (2002) Ca^{2+} dynamics in the lumen of the endoplasmic reticulum in sensory neurons: direct visualization of Ca^{2+} -induced Ca^{2+} release triggered by physiological Ca^{2+} entry. *EMBO J* 21:622–630.
- Tamamaki N, Nojyo Y (1991) Crossing fiber arrays in the rat hippocampus as demonstrated by three-dimensional reconstruction. *J Comp Neurol* 303:435–442.
- Toth K, Suares G, Lawrence JJ, Philips-Tansey E, McBain CJ (2000) Differential mechanisms of transmission at three types of mossy fiber synapse. *J Neurosci* 20:8279–8289.
- Turecek R, Trussell LO (2001) Presynaptic glycine receptors enhance transmitter release at a mammalian central synapse. *Nature* 411:587–590.
- Verkhratsky A (2005) Physiology and pathophysiology of the calcium store in the endoplasmic reticulum of neurons. *Physiol Rev* 85:201–279.
- von Gersdorff H, Borst JG (2002) Short-term plasticity at the calyx of Held. *Nat Rev Neurosci* 3:53–64.
- Zalutsky RA, Nicoll RA (1990) Comparison of two forms of long-term potentiation in single hippocampal neurons. *Science* 248:1619–1624.
- Zipfel WR, Webb WW (2001) In vivo diffusion measurements using multiphoton excitation fluorescence photobleaching recovery and fluorescence correlation microscopy. In: *Methods in cellular imaging* (Periasamy A, ed), pp 216–235. Oxford: Oxford UP.
- Zucker RS, Regehr WG (2002) Short-term synaptic plasticity. *Annu Rev Physiol* 64:355–405.